Solar Energy 137 (2016) 463–476

Contents lists available at ScienceDirect

Solar Energy

journal homepage: www.elsevier.com/locate/solener

On-sun operation of a 150 kW_{th} pilot solar receiver using dense particle suspension as heat transfer fluid

I. Perez Lopez [a], H. Benoit [a], D. Gauthier [a], J.L. Sans [a], E. Guillot [a], G. Mazza [b], G. Flamant [a,*]

[a] Processes, Materials and Solar Energy laboratory (PROMES-CNRS), 7 rue du Four Solaire, 66120 Font-Romeu Odeillo, France
[b] Institute for Research and Development in Process Engineering, Biotechnology and Alternative Energies (PROBIEN, CONICET – UNCo), 1400 Buenos Aires St., 8300 Neuquén, Argentina

ARTICLE INFO

Article history:
Received 24 February 2016
Received in revised form 22 June 2016
Accepted 22 August 2016
Available online 3 September 2016

Keywords:
Concentrated solar energy
High temperature solid particle receiver
Pilot scale experiment
Thermal efficiency

ABSTRACT

Previous studies proved the Dense Particle Suspension (DPS) - also called Upward Bubbling Fluidized Bed (UBFB) - could be used as Heat Transfer Fluid (HTF) in a single-tube solar receiver. This article describes the experiments conducted on a 16-tube, 150 kW_{th} solar receiver using a dense gas-particle suspension (around 30% solid volume fraction) flowing upward as HTF. The receiver was part of a whole pilot setup that allowed the continuous closed-loop circulation of the SiC particles used as HTF. One hundred hours of on-sun tests were performed at the CNRS 1 MW solar furnace in Odeillo. The pilot was tested under various ranges of operating parameters: solid mass flow rate (660–1760 kg/h), input solar power (60–142 kW), and particle temperature before entering the solar receiver (40–180 °C). Steady states were reached during the experiments, with continuous circulation and constant particle temperatures. For the hottest case, the mean particle temperature reached 430 °C in the collector fluidized bed, at the receiver outlet, and it went up to 700 °C at the outlet of the hottest tube, during steady operation. A temperature difference between tubes is observed that is mainly due to the incident solar flux distribution heterogeneity. The thermal efficiency of the receiver, defined as the ratio of power transmitted to the DPS in the form of heat over solar power entering the receiver cavity, was calculated in the range 50–90% for all the experimental cases. The system transient responses to variations of the solar irradiation and of the solid mass flow rate are also reported.

1. Introduction

Relying on new low carbon content power sources is the only long-term solution to meet with the growing worldwide population and the related energy demand increase but with low green house gas emission. Indeed, fossil fuels and nuclear power are harmful to the environment and their availability is limited. Oppositely, renewable energy sources present the advantage of being indefinitely available and they can be harvested in environmentally respectful ways with some technologies able to provide firm and dispatchable energy to the electricity grid.

Wind power and photovoltaic (PV) are already mature and cost effective technologies. In Spain for example, in 2014, wind power and solar PV represented 26.7% of the installed power and covered 23.4% of the yearly energy demand and 34.5% of the peak demand (REE, 2015). However the main drawback of both these technologies is their intermittence and unpredictability. Concentrated Solar Power (CSP) presents the distinctive advantage of dispatchability, based on its capability for thermal energy storage (International Energy Agency, 2011). Indeed, CSP Plants can store solar power in the form of heat that is transformed into electricity to cover the evening peak demand. In Spain, CSP represents 2.2% of the installed power, and in 2013 the CSP maximum instantaneous contribution was 7.6%, its maximum daily and monthly contributions were 4.6% and 3.6%, respectively (Technology Road Map, 2014). In Spain, the installed CSP increased by 17% from 2012 to 2013, allowing a 29% yearly contribution increase in that period (REE, 2014).

1.1. CSP operational plants current state

In 2014, 95.7% of the CSP operational plants were based on Parabolic Trough Collectors (PTC), whereas PTC technology only represented 73.4% of the under-construction projects (Baharoon et al., 2015). PTC is the most mature CSP design (Barlev et al., 2011), albeit the thermodynamic efficiency of associated power block is lower than 35% (Fernández-García et al., 2010) due to the operating temperature that is below 400 °C. In the past two years, the Solar Power Tower (SPT) technology started blooming with hundreds of MW_{th} installed (SolarReserve; BrightSource).

* Corresponding author.
E-mail address: gilles.flamant@promes.cnrs.fr (G. Flamant).

http://dx.doi.org/10.1016/j.solener.2016.08.034
0038-092X/

Nomenclature

Abbreviations

ColFB	collector fluidized bed
CoolFB	cooling fluidized bed
CSP	concentrating solar power
CSP2	"Concentrated solar power in particles" European project
DiFB	dispenser fluidized bed
DPS	dense particle suspension
DNI	direct normal irradiation (W/m^2)
HTF	heat transfer fluid
PID	proportional integral derivative

Latin symbols

$c_{p,p}$	particle specific heat (J/kg.K)
F_p	particle mass flow rate (kg/s)
G_p	particle mass flux (kg/m^2.s)
S	cavity aperture area (m^2)
T	temperature (°C)
$T_{p,DiFB}$	particle temperature in the dispenser fluidized bed (°C)
$T_{p,ColFb}$	particle temperature in the collector fluidized bed (°C)
$T_{p,i}$,	mean particle temperature at the cavity inlet (°C)
$T_{p,o}$	mean particle temperature at the cavity outlet (°C)
$T_{w,o}$	mean wall temperature at the tube outlet (°C)
$T_{tubes\ surface}$	average of all tube wall temperatures (°C)
U_{mf}	minimum fluidization velocity (m/s)
U	superficial velocity (m/s)
u	average velocity (m/s)

Greek symbols

ΔP	pressure drop (Pa)
$\Delta P/L$	linear pressure drop (Pa/m)
$\Delta T_{p\ ColFB\text{-}DiFB}$	temperature increase between the DiFB and ColFB (°C)
$\Delta T_{p\ hottest\text{-}coldest\ tube}$	particle temperature difference between the coldest and the hottest tubes at the tubes' outlet (°C)
$\delta\Delta T_{pColFB\text{-}DiFB}$	time-variation of the temperature increase between DiFB and ColFB (°C/min)
ε	*void fraction*
η_{th}	thermal efficiency
μ_g	gas viscosity (Pa.s)
ρ_g	gas density (kg/m^3)
φ_r	average solar flux density at the cavity aperture, referred to a 1000 W/m^2 DNI (W/m^2)
ϕ_{DPS}	power transmitted to the particles (W)
ϕ_{in}	inlet solar power at the cavity aperture (W)

It requires less land and less cooling water than PTC for a given electrical power output, due to higher cycle efficiency (Zhang et al., 2013) achieved thanks to higher operating temperature (higher than 500 °C). Moreover, SPT are less sensitive to seasonal variations than PTC linear systems (Technology Road Map, 2014). Nonetheless, in order to reduce the cost of the electricity produced by SPT power plants, high temperature receivers must be developed (Ho and Iverson, 2014).

In SPT plants, the heat is absorbed by a Heat Transfer Fluid (HTF). One of the key points to improve the SPT global efficiency, and therefore reduce the Levelized Electricity Cost (LEC), is the development of high temperature HTFs to power high efficiency thermodynamic cycles (Dunham and Iverson, 2014). Increasing the heat storage density also leads to cost reductions (Spelling et al., 2015). Therefore, high temperature HTFs, usable as both heat transfer and heat storage media (direct heat storage), are especially appreciated. Industrial SPT plants that include thermal storage are relatively new: the first plant operation started in 2007 (PS10, Spain), the first industrial plant with large-scale heat storage capacity, started production in 2011 (Gemasolar, Spain). Seven more industrial plants that include thermal storage are currently under development or under construction, with capacities ranging from 50 to 270 MW_e. The most advanced projects should start operational production in 2017 (NREL data base). Molten salt technology is the selected solution for this generation of SPT.

Molten salt is a very attractive technology because it allows operating at about 550 °C with direct thermal energy storage. Nevertheless, in mid to long terms following issues must be taken into account:

- The upper temperature of the salt (565 °C) is quite well-suited for a sub-critical steam Rankine cycle, but does not allow novel higher temperature cycles such as supercritical steam cycles, supercritical CO_2 Brayton cycles, or gas turbines used in recuperated or combined cycles.
- The risk of salt solidification (220–240 °C) is manageable as proven by the routine operation of the Gemasolar plant, but remains a strong operation constraint.

Consequently, new concepts need to be developed that maintain the advantages of molten salt but open the route to higher operation temperature. Particle receivers are among the alternatives (Ho and Iverson, 2014) and this paper deals with the fluidized particles-in-tube concept.

1.2. Fluidized particles-in-tube concept for concentrated solar power

Bubbling gas-particles fluidized beds have been largely developed as heat exchangers, although in these particles are not used to transport or store energy. Circulating fluidized beds are used industrially in drying, combustion and catalytic gas-solid reactions, but due to their high voidage the energy transfer between the bed walls and the particles is low. Moreover, they require a high gas mass flow rate that consumes energy (parasitics).

A new concept, the so-called Upward Bubbling Fluidized Bed (UBFB), which involves a Dense Particle Suspension (DPS) (around 30% solid volume fraction) circulating upward in vertical tubes, was developed jointly by LGC-INPT/CNRS and PROMES-CNRS (Flamant and Hémati, 2010). Applied as a Heat Transfer Fluid (HTF) in solar receivers, this technology presents the advantages of high solid fraction and mass flow control. In addition, particles can be used as the heat storage medium for direct thermal energy storage. The concept was patented (Flamant and Hémati, 2010) and its validity was proven with on-sun batch operation of a single-tube experimental solar receiver (Flamant et al., 2013). Furthermore, Benoit et al. (2015) did achieve DPS outlet temperatures higher than 750 °C and calculated heat transfer coefficients up to 1100 W/m^2.K by using the same single-tube solar rig.

This paper presents the second step of this innovative technology development: the first experimental results of on-sun test campaigns on a 150 kW_{th} multi-tube pilot solar rig operating in closed circuit. This pilot loop was developed in the frame of the CSP2 FP7 European project (CSP2 Project, 2015).

The objectives of the experimental tests of the 16-tube solar rig, which was comprised of all the main elements (or equivalent) of a real plant, were the following:

- Closed loop particle circulation through all the components of the solar rig;
- Solid mass flow rate control under various ranges of parameters;
- 700 °C particle temperature at the solar receiver outlet (at least for some receiver tubes);
- High thermal efficiency (at least 75%).

2. Experimental setup

2.1. Particles

The properties of the SiC particles used in the experiments are indicated in Table 1. They were selected for their good thermal properties and the Sauter diameter of 64 μm was chosen in order to have a Geldart-Baeyens type-A easily fluidized powder (Geldart, 1973).

2.2. Description of the experimental solar loop

Experiments were carried out on a solar rig that was comprised of the main elements of a real SPT plant. COMESSA Company managed the detailed engineering arrangement and built the pilot rig. The rig was set at the focus of the CNRS 1 MW solar furnace at Odeillo, France. The pilot solar loop is schemed in Fig. 1. Two rotary valves (1) and (3) control the inlet and outlet of particle in the cold storage tank (2). An Archimedes screw conveyor (4) feeds SiC particles of diameter 64 μm issued through a controlling rotary valve (3) from the bottom of the storage tank (2) -hopper- to the Dispenser Fluidized Bed (DiFB) (5), where they are fluidized. Because of the overpressure in the DiFB (hydrodynamics of this concept is detailed in Boissière et al. (2015)) the DPS rises up the 16 identical vertical absorber tubes (6) (i.d. 29.7 mm, thickness 2 mm, 2.27 m height, with 1 m length exposed to the concentrated irradiation) set inside the solar receiver cavity (7). The sun-heated tubes transmit the absorbed energy to the particles. A gas injection nozzle is set on each tube, 0.53 m above the tube bottom for aeration (11).

Table 1
Properties of SiC particles.

ρ_p (kg/m^3)	$\rho_p C_{p,p}$ (at 250 °C) (kJ/m^3.K)	$T_{sintering}$ (°C)	Shape factor	Sauter diameter (μm)
3210	3000	1620	0.77	63.9

Particles leaving the tubes at their upper section are all collected in the Collector Fluidized Bed (ColFB) (8), where their temperature is homogenized. Then, the DPS can be water-cooled in the Cooling Fluidized Bed (CoolFB) (9). At the CoolFB outlet, particles are conveyed into the storage tank by a recycling screw conveyor (10). During on-sun experiments conducted in closed loop circulation, the complete load of the rig was 900 kg of SiC particles.

Fig. 2 displays a 3D view of the CSP2 pilot unit. The ColFB and the storage tank are equivalent to the hot and cold storage of a real plant, respectively, the CoolFB corresponds to the heat exchanger, although in this solar rig it is used to adjust the particle temperature.

A horizontal cross-sectional view of the cavity with the 33.7 mm e.d. tubes is shown in Fig. 3. The cavity is 1 m high and its aperture (located at the bottom of Fig. 3) is 0.15 m wide and 0.5 m high.

2.3. Instrumentation

The pilot rig instrumentation was comprised of 126 instruments (pressure and differential pressure sensors, thermocouples, gas and solid mass flow meters, valves and security switches). Each fluidized bed was equipped with a differential pressure sensor, and two pressure sensors located in the freeboard and in the plenum, respectively. The particle temperature in the DiFB was measured with four K thermocouples placed at the bottom and at middle height of the bed, at both the East and West sides. The CoolFB was equipped with one K thermocouple for solid temperature measurement. The solar receiver cavity was inside-insulated by high temperature micro-porous modules. A differential pressure sensor measured the pressure drop of each tube. K thermocouples were set to measure the DPS and wall temperatures of the tubes. The rear tube wall temperature at the tube middle height and the solid outlet temperature were measured on all tube. In addition, for six selected tubes (1, 4, 8, 9, 13, 16), the rear wall temperature and the solid temperature were also measured at the irradiated cavity inlet and outlet. The three rear wall thermocouples are placed 10 mm from the bottom and top insulation plates and in the middle of the six tubes (0.5 m from the bottom). Fig. 4 displays the main instrumentation and its location. On this screen printing of the pilot rig flow sheet, T_p represents a DPS temperature sensor, T_w a wall temperature sensor and P and ΔP correspond to absolute and differential pressure sensors, respectively. The line and arrows indicate the particle circulation.

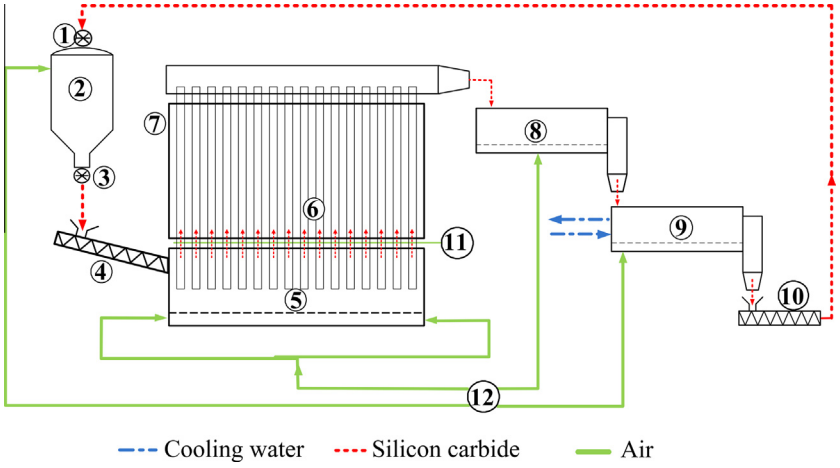

Fig. 1. Schematic view of the pilot solar loop: ① Rotary valve 1, ② Storage tank, ③ Rotary valve 2, ④ Feeding screw conveyor, ⑤ Dispenser fluidized bed, ⑥ Irradiated tubes, ⑦ Receiver cavity, ⑧ Collector fluidized bed, ⑨ Cooling fluidized bed, ⑩ Recycling screw conveyor, ⑪ Aeration, ⑫ Compressed air supply.

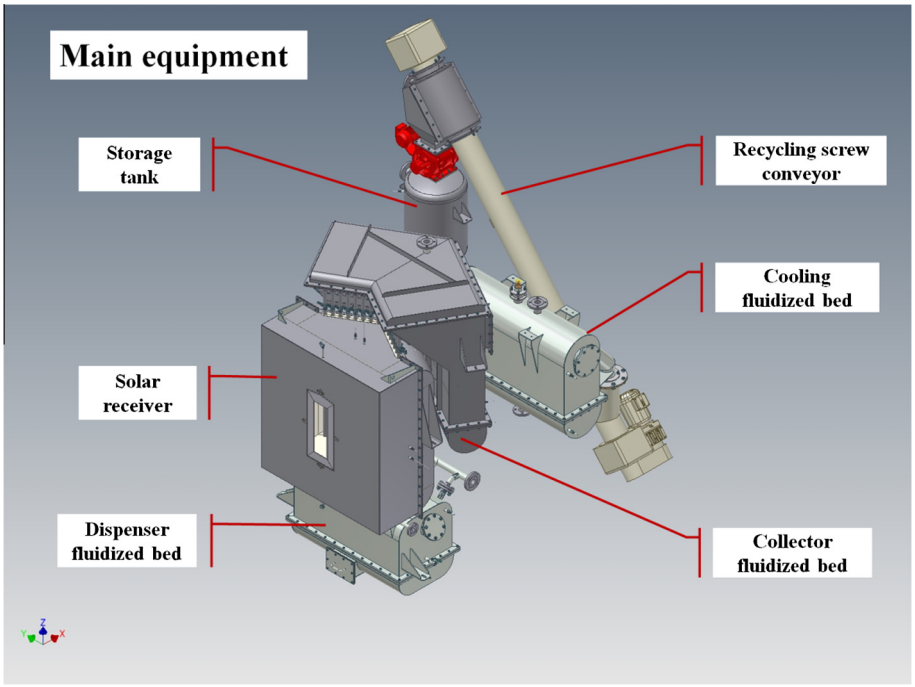

Fig. 2. 3D view of the pilot solar loop (source COMESS).

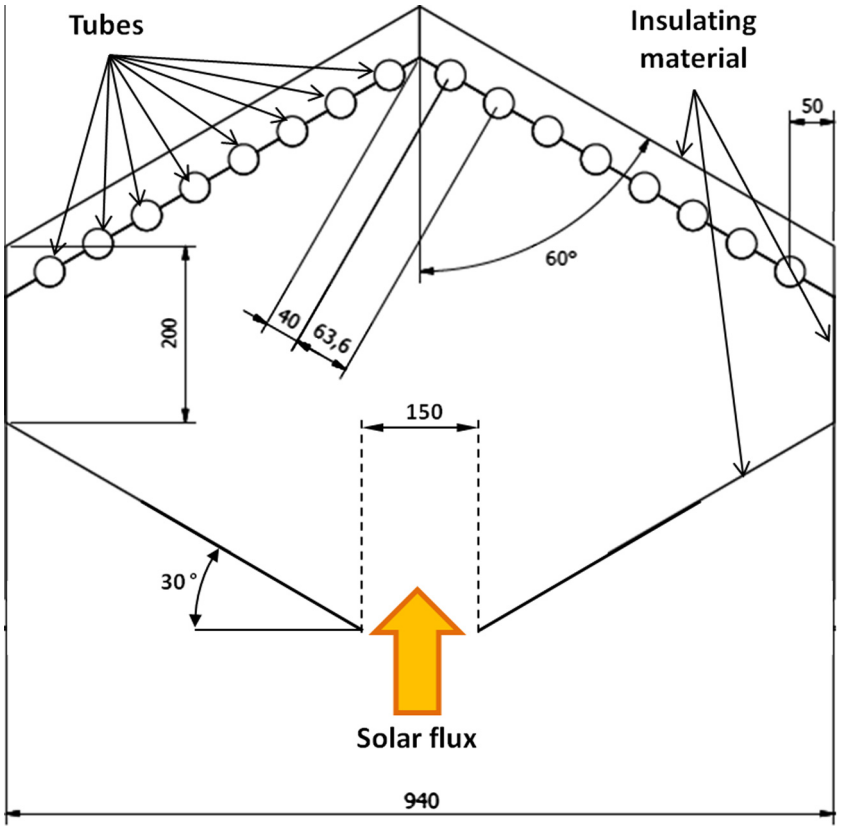

Fig. 3. Horizontal cross-sectional view of the receiver cavity (size in mm).

2.4. Solar furnace qualification

The CNRS 1 MW solar furnace at Odeillo is a double reflection facility that involves 63 flat heliostats (6 m high and 7.5 m wide, 45 m^2 area each, 2835 m^2 total area), facing south, and positioned on 8 terraces (5 m between each terrace). Heliostats reflect the solar rays parallel to the north-to-south/horizontal optical axis of the north-facing parabola (40 m high, 55 m wide, 18 m focal

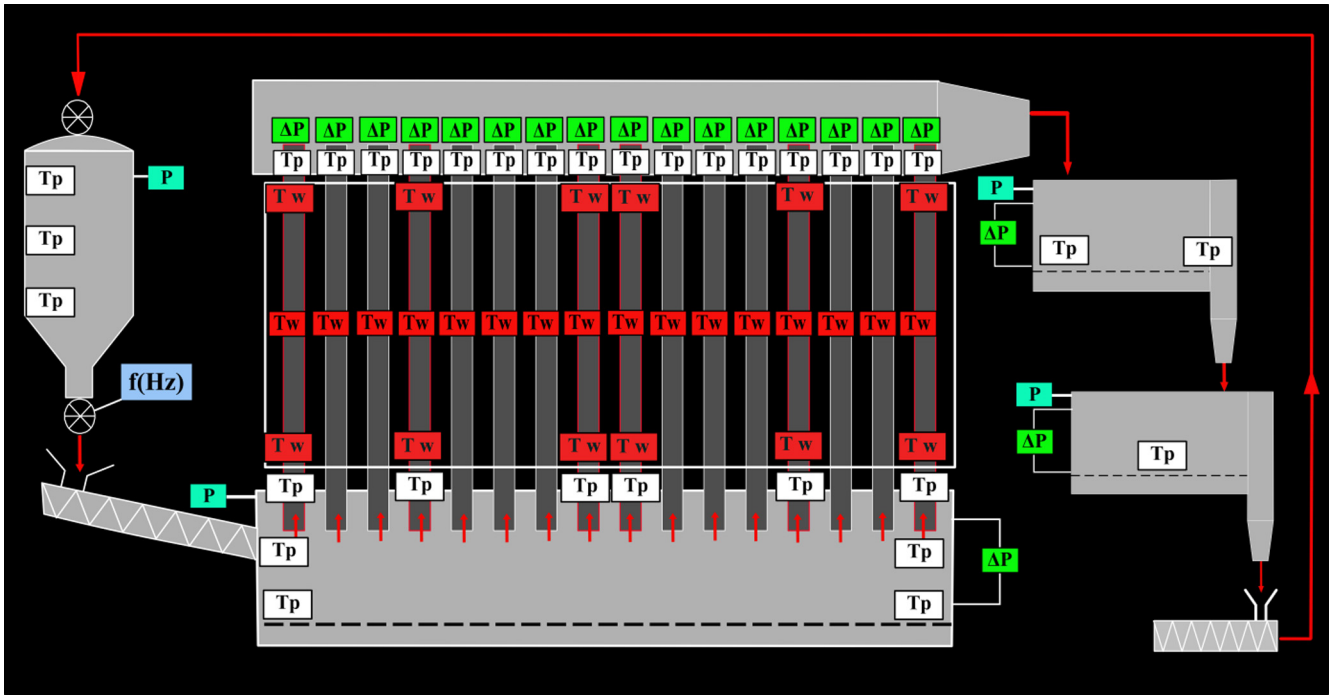

Fig. 4. Main instrumentation of the pilot plant (T_w wall temperature thermocouples, T_p particle temperature thermocouples, P pressure sensors, ΔP differential pressure sensors, f(Hz) rotary valve frequency regulator.

length). Thanks to this double reflection, all solar rays impinging on the heliostats are concentrated at the focus of the parabola where the experimental setup is installed.

Three groups of heliostats were chosen in the field, providing an actual inlet power at the receiver aperture ranging from 63 to 142 kW_{th}, which corresponds to a mean solar flux density in the range 1–1.8 MW/m^2 at the rectangular receiver aperture. The tubes were irradiated through a 15 × 50 cm slot. Due to the specificities of this parabolic solar furnace, designed for very high flux at the focal point (concentration about 9000), an uneven flux distribution at the cavity entrance was expected. Consequently, the tracking reference position (azimuth and elevation) of the selected heliostats was modified in order to obtain a homogeneous solar flux distribution at the receiver aperture.

For each of the three solar field settings, the solar power measurement at the cavity aperture was carried out using a calorimeter (24.7 mm diameter, 18.8 mm^2 area) set at 33 different positions on a board located at the cavity entrance (see Fig. 5). Each measurement was realized over at least one hundred seconds, with one value taken every second. The values presented are time averages of all the instantaneous values. The variations of instantaneous values due to wind on the heliostat field were less than 8% of the average over time. The measurements were normalized.[1] The DNI was continuously measured to be able to determine the solar flux density at any time, at every sensor position, for the three solar field settings.

Table 2 gives for all three settings the number of heliostats, the mean value of the normalized flux density at the cavity aperture (average of the 33 measurements), the inlet power and the sample standard deviation of flux density divided by the average value of the 33 measurements (= flux variation coefficient). This last coefficient gives an indication of the flux density homogeneity at the cavity aperture for each heliostat field setting.

[1] The normalized flux density is the flux density that would have been measured for a DNI of 1 kW/m^2.

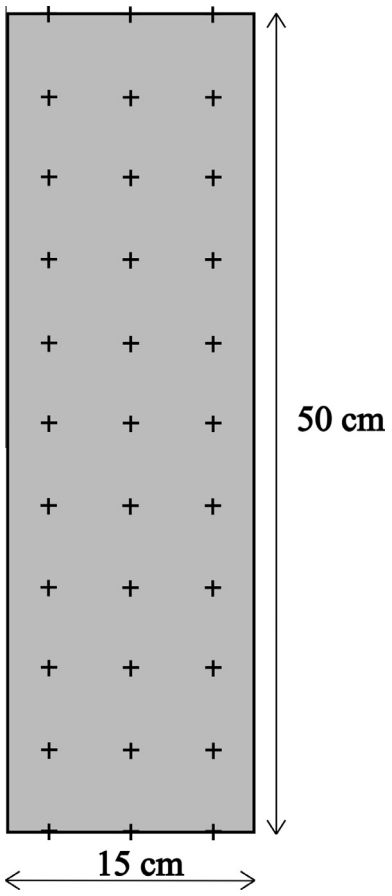

Fig. 5. Cavity slot surface (grey) and calorimeter measurement positions (black).

Fig. 6 displays the solar flux density maps at the cavity aperture, obtained by interpolating the measurements, for each heliostat field setting.

Table 2
Normalized (referred to a 1000 W/m^2 DNI) inlet power and flux density at the cavity entrance for each heliostat field setting.

Setting	Number of heliostats	Normalized mean solar flux density at the cavity entrance (kW/m^2)	Flux variation coefficient	Normalized inlet power at the cavity entrance (kW$_{th}$)
		1048	13%	78.6
A		1048	13%	78.6
B	27	1429	2%	107.2
C	32	1772	1%	132.9

Another set of solar flux density distribution measurement was done with a fluxmeter inserted in the back wall of a mock-up cavity (without tubes) at 41 positions. The mock-up cavity has the same shape as the pilot plant cavity and is 5 cm smaller in height and width. Its inside walls are covered in a material similar to that insulating the actual cavity. Measurements have been performed by opening and closing rapidly the front doors of the solar furnace in order to limit the temperature increase of the mock-up walls. Fig. 7 is a photograph of the mock-up cavity back, installed behind a protective shield at the focus of the solar furnace. On this photograph, white spots correspond to the fluxmeter positions. Flux density maps at the cavity back wall can be obtained by interpolating the measured values. This flux measurement setup was used for several solar furnace configurations, among which one is very similar to setting C (35 heliostats shooting instead of 32, 1.94 MW/m^2 average flux density in the center instead of 1.82 MW/m^2, same doors' opening). The interpolated flux map of the furnace setting similar to setting C is shown in Fig. 8. We can observe that the flux density was far from homogeneous when considered out of the focal plane. The reversed shadow of the focal tower leads to a low solar flux zone in the middle of the back wall upper part. The solar flux density varies by a factor of 3 between the low flux density zones (150 kW/m^2) and the high flux density zones (500 kW/m^2). This solar flux map will obviously induce cold and hot spots during testing of the solar receiver.

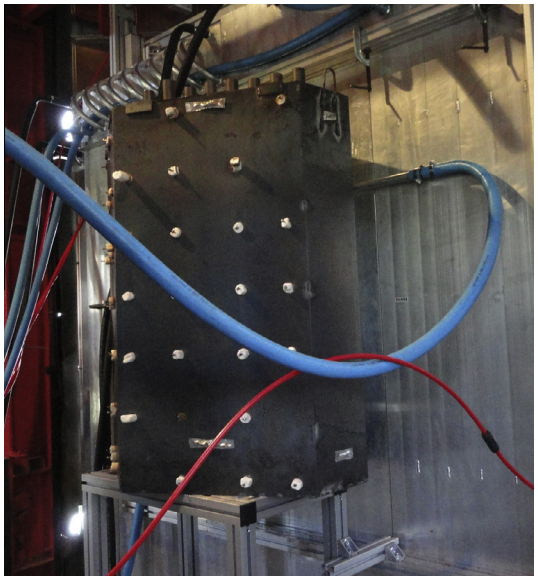

Fig. 7. Back photograph of the mock-up cavity (white dots = fluxmeter positions).

2.5. Experimental procedure

For any experiment, a heliostat field setting (A, B or C) was first chosen and was kept during the whole experiment. Then, compressed air was injected in all fluidized beds (for fluidization) and in the receiver tubes (for their aeration). An additional air flow rate was injected in the DiFB freeboard for pressure control needs (to compensate for the system's air leakage and allow reaching the desired pressure). The PID (proportional-integral-derivative) control valve, controlling the DiFB freeboard pressure, was operated either manually (valve opening setting) or in automatic mode (DiFB pressure setting). To induce the particle circulation, the pressure control valve was progressively closed, making the pressure increase and the DPS rise in the vertical absorber tubes until particles reached the outlet. Then the rotary valve frequency was preset to get the desired solid mass flow rate (rotary valve previously calibrated). The closed loop circulation was finally obtained by launching the feeding screw, the rotary valve #2 set at the tank outlet, then the rotary valve #1 and finally the recycling screw conveyor. Next, the cavity was progressively heated by opening partially the solar focus doors. When the cavity temperature increase slowed down, the doors were opened to correspond to

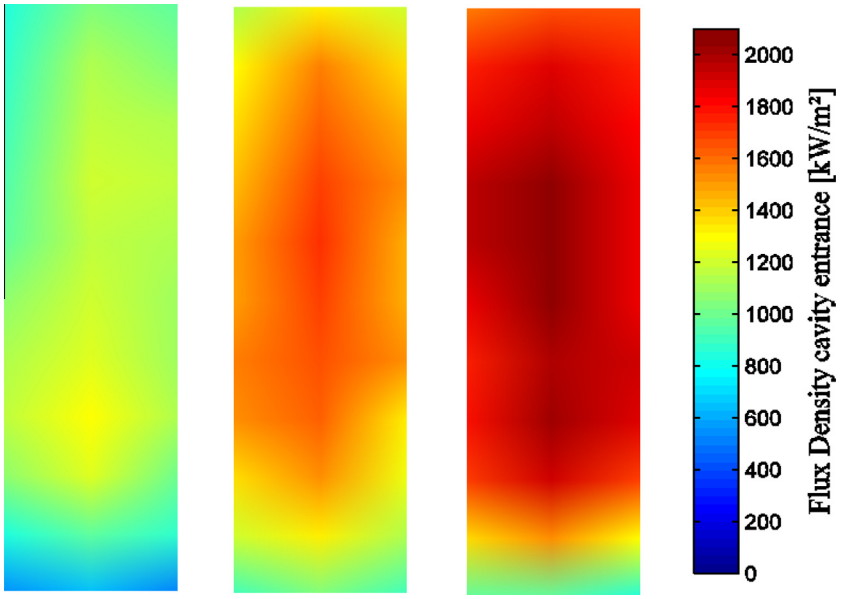

Fig. 6. Flux density distribution at the cavity entrance for the 3 heliostat field settings (left = setting A; middle = setting B; right = setting C), normalized for a 1000 W/m^2 DNI.

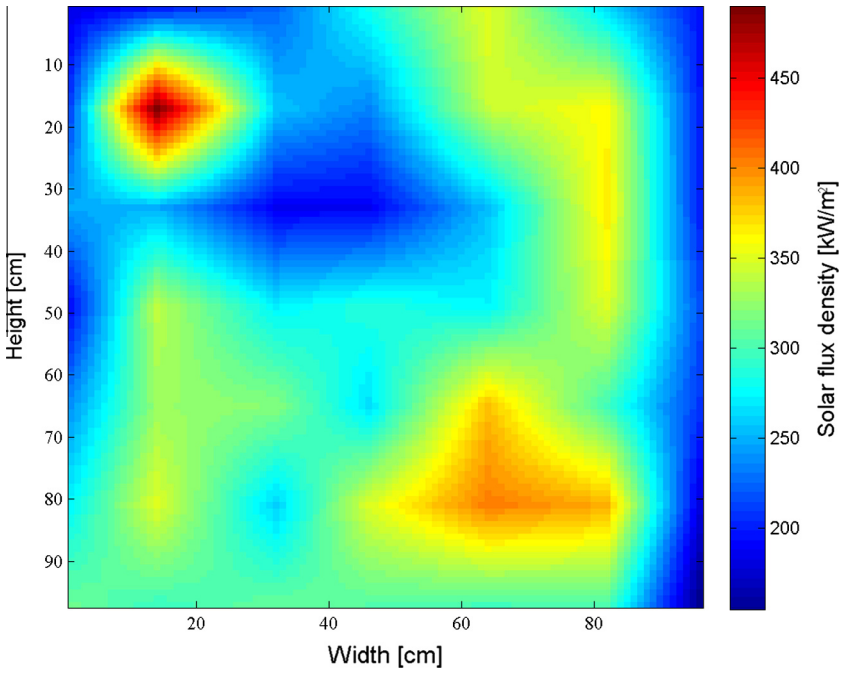

Fig. 8. Solar flux density map at the back wall of the mock-up cavity for a furnace setting similar to setting C.

Table 3
Ranges of operating parameters.

Inlet solar power (kW_{th})	F_p (kg/h)	G_p (kg/m^2.s)	$T_{p,DiFB}$ (°C)	Aeration flow rate (N m^3/m^2.s)	Fluidization flow rate DiFB (N m^3/m^2.s)	Fluidization flow rate ColFB (N m^3/m^2.s)	Fluidization flow rate CoolFB (N m^3/m^2.s)
63–142	662–1759	17–44	43–184	0.09	0.013	0.010	0.010

Table 4
Range of particle residence time and air superficial velocities in normal conditions (0 °C, 1.013 bar).

Mean residence time of the particles in the receiver tubes	Aeration velocity	Fluidization velocity in the DiFB	Fluidization velocity in the ColFB and CoolFB
73–229 s	0.09 m/s = 18 U_{mf}	0.013 m/s = 2.6 U_{mf}	0.01 m/s = 2 U_{mf}

the furnace setting selected. Finally, when on-sun particle circulation was well established, the operator maintained a constant solid mass flow rate until all temperatures stabilized, thus achieving steady state. After a reasonable time at steady state, a new rotary valve frequency could be imposed, in order to get another mass flow rate to reach another steady state.

3. Analysis of the pilot solar receiver performances

More than 100 h of on-sun experiments were performed. Several on-sun experiments were discarded because steady state was not reached, due to meteorological conditions or technical issues. Finally, 29 experiments reached steady state (see definition in §3.2) whose durations ranged between 16 and 110 min.

3.1. Operating parameters and ranges of experimental results

The main system operating parameters were the solar power at the cavity aperture, the particle flow rate, and the particle temperature in the DiFB. The aeration flow rate was set to 0.09 N m^3/m^2.s for all tubes during all experiments. It corresponds to the maximum aeration value tested previously (Flamant and Hémati, 2010) that was chosen to ensure a good circulation in all tubes. Indeed, a tube without circulation would risk overheating and getting damaged. The security was privileged over the effect the aeration might have on the heat transfer coefficient. The inlet power at the cavity aperture ranged from 63 to 142 kW_{th}, which corresponds to a mean solar flux density in the range 1–1.8 MW/m^2. The solid mass flow rate was varied from 600 to 1800 kg/h, and the corresponding mass flux from 17 to 44 kg/m^2.s. The solid mass flux was limited to the maximum allowed by the rotary valve and not by the process itself. As shown by Turzo (2013), the solid flux can be as high as 700 kg/m^2.s for the DPS upward flow in tube technology (in i.d. 28 mm tubes). The solid temperature in the DiFB varied from 43 to 184 °C. It was controlled through a water-cooling coil immersed in the CoolFB. Table 3 displays the operating parameter ranges. F_p is the solid mass flow rate, G_p is the solid mass flux (flow rate divided by circulation section area), $T_{p,DiFB}$ is the particle temperature in the DiFB.

Table 4 indicates the particle residence time range in the 1 m high irradiated part of a tube (related to the solid mass flow rate), the aeration air superficial velocity in the tubes and the fluidization velocities in all fluidized beds, calculated for normal conditions (P = 1.013 bar et T = 0 °C). The velocities are also given as a ratio with respect to the minimum fluidization velocity (U_{mf} = 5 mm/s at 20 °C and 1.013 bar, Thonglimp et al., 1984).

The air superficial velocity in actual operating conditions depends on the temperature that affects the air properties (density and viscosity). For small particles, inertia is the dominant parameter governing gas-particle interactions, consequently, the

Table 5
Experimental result ranges.

$\Delta T_{p,DiFB\text{-}ColFB}$ (°C)	$T_{tubes\ surface}$ (°C)	$T_{p,i}$ (°C)	$T_{p,o}$ (°C)	T_{ColFB} (°C)	$\Delta P/L$ in tubes (Pa/m)
137–335	366–625	69–251	217–495	188–433	11 340–11 780

Table 6
Steady state experimental data (Φ_{in} = solar power entering the receiver cavity, F_p = solid mass flow rate, $T_{DiFB\ mean}$ = mean temperature in the DiFB, $T_{p,o\ mean}$ = average of the tube outlets temperatures, $T_{ColFB\ mean}$ = mean temperature in the ColFB; Φ_{DPS} = power absorbed by the particles).

Φ_{in} (kW)	F_p (kg/h)	$T_{DiFB\ mean}$ (°C)	$T_{p,o\ mean}$ (°C)	$T_{ColFB\ mean}$ (°C)	Φ_{DPS} (kW)
63	1462	51	217	188	45
69	1205	60	261	236	49
68	1286	53	254	217	49
71	1396	54	248	222	54
69	1196	58	272	245	53
71	1027	60	296	265	50
74	662	65	353	308	39
76	1196	82	291	277	56
78	801	52	336	290	46
82	1423	65	270	247	61
74	1455	145	334	303	58
79	983	59	319	286	53
80	872	44	330	280	49
80	1526	105	321	270	61
141	1746	91	371	317	97
129	1707	59	339	277	89
142	1401	123	442	391	97
84	974	132	417	359	57
98	847	90	403	360	57
139	1207	127	451	413	90
106	1662	43	297	238	76
104	1244	102	369	331	71
85	716	184	495	412	44
108	1439	105	359	321	78
112	1061	84	422	383	80
105	825	98	473	433	72
109	1759	83	370	309	98
109	1746	96	353	310	92
107	1713	66	310	271	84

minimum fluidization velocity decreases with air viscosity (According to Thonglimp's correlation (Thonglimp et al., 1984) the minimum fluidization velocity is U_{mf} = 2.7 mm/s at 400 °C and 1.25 bar). It was observed thanks to helium tracking experiments that the slip velocity ($u_{slip} = u_{air} - u_p$) between phases at the tube inlet in the DiFB is close to the slip velocity at the minimum fluidization (Boissière et al., 2015). When the solid flow rate entering the tube is set, the solid average velocity is known ($u_p = F_p/(\rho_p.S_{tube})$), and the air superficial velocity at the tube inlet $U_{air,inlet}$ is calculated with the equation:

$$U_{air,inlet} = u_{air,inlet} \times \varepsilon_{inlet} = (u_p + u_{slip})_{inlet} \times \varepsilon_{mf} = (u_p + u_{mf}) \times \varepsilon_{mf} \quad (1)$$

Therefore, the total air flow rate in a tube can be determined by adding the aeration flow rate to the air flow rate entering with the solid at the tube inlet. In normal conditions, the air flow rate in a tube corresponds to an air superficial velocity U_{air} of 0.105 m/s for a 25 kg/m^2.s solid flux (that is 1000 kg/h in 16 tubes). This includes the air flow entering the tube inlet. In all explored conditions (temperature and solid flow rates), the air superficial velocity in the system remained below 0.2 m/s. This low air velocity leads to negligible particle attrition due to inter-particle collisions and particle-to-wall impacts (negligible when superficial gas velocities are lower than 30 m/s (Zhang et al., 2016).

Table 5 gives the ranges of experimental results: temperature increase between DiFB and ColFB ($\Delta T_{p,DiFB\text{-}ColFB}$), average of the measured tubes' wall temperatures ($T_{tubes\ surface}$), average of the particle temperatures measured in the tubes at the cavity inlet ($T_{p,i}$) and cavity outlet ($T_{p,o}$), temperature in the ColFB (T_{ColFB}) and linear pressure drop in the tubes ($\Delta P/L$). The pressure drop in the tubes is in the range 11 340–11 780 Pa/m, which is mainly due to the particle weight with a small contribution of the wall-particle friction that is function of the solid mass flux (Boissière, 2015).

The maximal particle temperatures reached at the tubes' outlets during steady states and transient periods. The average of the temperatures measured at the 16 tubes' outlets ($T_{p,o\ Mean}$) reached 495 °C during a steady state and 585 °C during a transient period. The temperature at the outlet of the hottest tube ($T_{p,o\ Hottest\ tube}$) reached 698 °C during a steady state and 585 °C during a transient period. The difference between the hottest tube outlet temperature and the average outlet temperature is due to the non-uniform solar flux density distribution on the tubes.

3.2. Steady state experiments selection

The first criteria to select the steady state experiments were the stability of the solid mass in the DiFB, which reflected the solid flow rate stability, and the temperature stability, evaluated through the particle temperature increase between the dispenser and the collector fluid beds ($\Delta T_{p,ColFB\text{-}DiFB}$). $\delta\Delta T_{p,ColFB\text{-}DiFB}$ is the time variation of this difference during steady state. Twenty-nine experiments were selected; their data are listed in Table 6. The highest value of $\delta\Delta T_{ColFB\text{-}DiFB}$ during all steady state runs was less than 1.6 °C/min, and for 21 experiments it was even less than 0.5 °C/min. The stable periods durations ranged from 16 to 108 min. Twenty steady state experiments, with stable irradiation conditions, were selected for calculating the thermal efficiency (η_{th}).

3.3. Particle suspension temperature during steady state

Outlet DPS temperature around 750 °C and 250 °C particle temperature increase was achieved with a single-tube solar receiver in Benoit et al. (2015). Actually, the particle outlet temperature could not overpass 750 °C since the stainless steel tube had to remain below 900 °C for safety reasons. Thermocouples were set at the hottest spots, on the front sides of 3 tubes, to keep the temperature in check. In the present study, 693 °C was reached at the outlet of at least one tube, and the mean temperature at the outlet of the 16 tubes reached 495 °C, with solar heating only (closed loop circulation). As explained before, the flux distribution in the cavity was uneven because of the solar furnace specificities (the incident solar flux on the various tubes may vary by a factor of at least 3), and therefore the temperature distribution was also uneven. A few tubes only were receiving enough irradiation to allow particles to reach high temperature. Actually, similarly to the single-tube solar receiver, the particle outlet temperature could not overpass 750 °C at the outlet of the hottest tubes because of the stainless steel tube limitation to about 900 °C. Consequently, this highest acceptable temperature constraint on the hottest tube surface results in lower particle temperature at the outlet of the tubes submitted to low solar irradiation. This is why the mean solid temperature at the receiver outlet is globally limited.

At the tube outlets, during the steady state periods, the particle temperature difference between the hottest tube and the coldest tube ($\Delta T_{p,hottest\text{-}coldest\ tube}$) was higher than 130 °C and it went up to 390 °C. $\Delta T_{p,hottest\text{-}coldest\ tube}$ for steady state experiments are given in Fig. 9. Neither the particle flow rate nor the inlet power at the cavity entrance has influence on the temperature difference between the hottest tube and the coldest tube, thus suggesting that it is mainly due to the incident solar flux heterogeneity on the receiver tubes. The solar furnace used as concentrating system in our experiments is the cause of this heterogeneity that would not exist in the case of a receiver set at the top of a solar tower.

Fig. 10 plots an example of measured particle mean temperatures at all tube outlets during a steady experimental run lasting 55 min and at the hottest moment of this experiment. The particle outlet temperature, averaged over the 16 tubes, was 442 °C. Fig. 11 shows the mean tube wall temperatures at the inlet, middle high and outlet of the 16 tubes for the experimental run displayed in Fig. 10: the relation between the particle temperature and the tube wall temperature is obvious since the hottest tubes are those with the hottest outlet particle temperatures while the other tubes at lower temperature have lower particle outlet temperatures. During

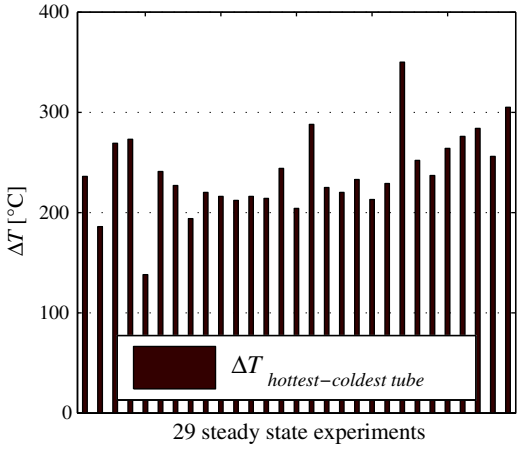

Fig. 9. DPS mean temperature difference between the hottest and the coldest tubes for each one of the steady state experiments.

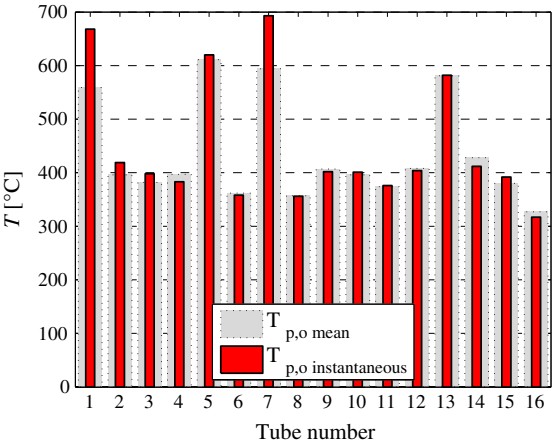

Fig. 10. Hottest solid temperature and mean solid temperature at the tube outlets during a 55-min steady experiment (aeration = 0.09 N m^3/m^2.s, mass flux = 35 kg/m^2.s and solar power at the cavity entrance = 142 kW_{th}).

the steady state periods, the particle temperature averaged over the 16 tube outlets reached 495 °C, while it was as high as 698 °C at the outlet of the hottest tube.

In this pilot scale facility, the solid flow rate was measured globally, and there was no individual measurement in the tubes. Although the sonic aeration nozzles were expected to distribute uniformly the aeration between the 16 tubes, the uniform distribution of the solid flow rate between all tubes was not ensured. In particular, the temperature difference between tubes can generate solid flow rate difference. But all particles leaving the irradiated cavity are collected in the ColFB, where their temperature is homogenized. Therefore we considered the temperature increase between the DiFB and the ColFB ($\Delta T_{p,ColFB\text{-}DiFB}$) as the reference temperature increase. Fig. 12 plots the temperature increase between the DiFB and the ColFB for the three considered heliostat field settings. The mean temperature increase between the DiFB and the ColFB ranges between 137 °C and 335 °C, with a mean value of 218 °C. The tube length between these 2 fluidized beds is 2.27 m, but only 1 m of the total length is irradiated. The maximal mean temperature increase, 335 °C, corresponds to an experiment with a 21 kg/m^2.s solid flow rate and a 105 kW_{th} inlet solar power at the cavity entrance. The minimum mean temperature increase, 137 °C, corresponds to an experiment with a 37 kg/m^2.s solid flow rate and a 63 kW_{th} inlet solar power. For the three considered inlet solar powers, it can be seen that the temperature increase $\Delta T_{p,ColFB\text{-}DiFB}$ decreases with the solid mass flux. Moreover, for a given solid mass flux, the higher the solar power at the cavity inlet, the higher the temperature increase.

3.4. Thermal efficiency

In concentrating power solar plants (CSP), the heliostat field represents one of the main capital costs. So, by reducing its size for a given plant capacity, the capital cost will be reduced. The experimental determination of the thermal efficiency (η_{th}) was one of the main objectives of this study, since it plays an important role in the plant performance improvement. The procedure, including the various influent parameters' calculation, is detailed hereafter.

3.4.1. Pertinent experiments' selection

Selected experiments for thermal efficiency calculation were those at steady state with stable mass flow rate and temperatures, and stable DNI conditions. Fig. 13 plots an example of a steady

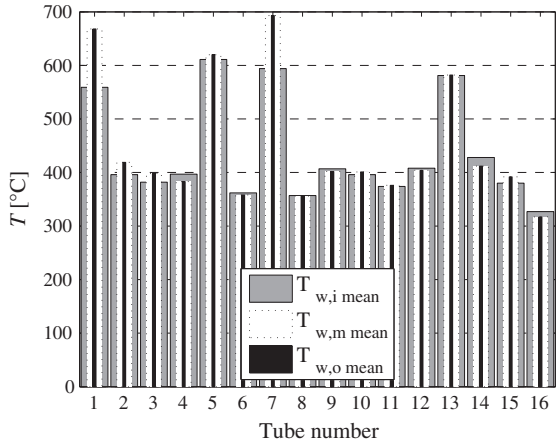

Fig. 11. Wall mean temperature distribution at various tube heights: inlet, middle and outlet during a 55-min steady experiment (aeration = 0.09 N $m^3/m^2.s$, mass flux = 35 $kg/m^2.s$ and solar power at the cavity entrance = 142 kW_{th}).

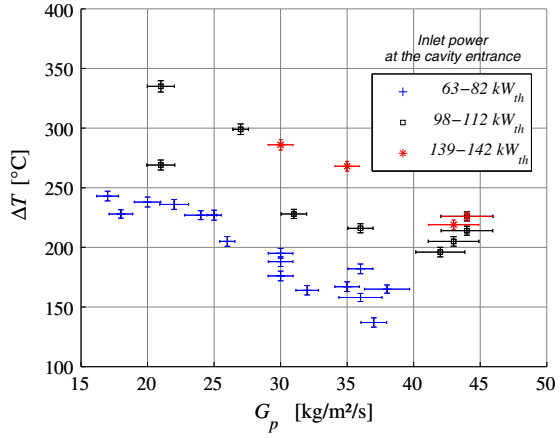

Fig. 12. Temperature increase between DiFB and ColFB as a function of the solid mass flux, for the three considered solar power ranges at the cavity entrance.

state experiment, with stable temperatures and mass flow rates, and appropriate irradiation conditions for thermal yield calculation.

3.4.2. Thermal efficiency calculation

The thermal efficiency is defined as:

$$\eta_{th} = \frac{\phi_{DPS}}{\phi_{in}} \tag{2}$$

where ϕ_{DPS} represents the power transmitted to the DPS (power extracted by the particles) and ϕ_{in} represents the solar power at the cavity aperture.

Three different settings of the heliostat field were chosen to have different inlet powers at the cavity aperture (0.15 m × 0.50 m slot). The inlet power for any experiment is calculated as:

$$\phi_{in} = \varphi_r \times \frac{DNI}{1000} \times S \tag{3}$$

with ϕ_{in} the solar power at the cavity inlet, φ_r the solar flux density averaged over the cavity aperture referred to a 1000 W/m^2 *DNI*, *S* the cavity aperture area and *DNI* the direct normal irradiation.

The extracted power is defined as:

$$\phi_{DPS} = F_p \int_i^{T_o} c_{p,p} dT \approx F_p \cdot \overline{c_{p,p}} \cdot (T_{p,ColFB} - T_{p,DiFB}) \tag{4}$$

with F_p the particle mass flow rate, $c_{p,p}$ the particle specific heat capacity, $T_{p,ColFB}$ the particle temperature in the collector fluidized bed, and $T_{p,DiFB}$ the temperature in the dispenser fluidized bed.

The air heat capacity is neglected in front of that of the solid. The latter is calculated with a polynomial expression established from the values given by the NIST database (Munro, 1997):

$$c_{p,p}(T_p) = aT_p^3 + bT_p^2 + cT_p + d \tag{5}$$

with T_p in K and $a = 2.25 \cdot 10^{-7}$ J/kg.K^4, $b = -9.88 \cdot 10^{-4}$ J/kg.K^3, $c = 1.62$ J/kg.K^2, $d = 320$ J/kg.K.

Temperatures used in the enthalpy balance were chosen as detailed hereafter. Since the process involves A-type powders (Geldart, 1973), the required gas flow rate and associated sensible heat losses are very low (Zhang et al., 2016). In this study with SiC particles, heat losses associated to the gas are negligible, always less than 2% of the power extracted by the suspension, consequently the heat balance was performed considering only the particle suspension enthalpy. As pointed out in Benoit et al. (2015) and García-Triñanes et al. (2016), a solid recirculation phenomenon occurs in the vertical tubes: most particles flow upward in the tube center region, whereas they flow downward near the tube wall. Therefore, in order to take into account the transferred heat to the particles going down into the DiFB, the temperature inlet considered for the enthalpy balance is the mean temperature of the four thermocouples set in the DiFB. This is indeed more logical than considering the mean temperature of the six measured tube inlets (tubes 1, 4, 8, 9, 13 and 16). Regarding the outlet particle temperature, all 16 tubes were equipped with thermocouples, but there is only one global measure of the particle flow rate. As mentioned, the solid mass flow rate uniform distribution between tubes was not ensured, which invalidates the use as outlet temperature of the average of the 16 tubes' outlet temperatures. The solid outlet temperature was taken as the mean of the indications of the two thermocouples placed in the collector fluidized bed, because of its homogenized temperature. This induces a thermal efficiency underestimation due to the ColFB heat losses.

The thermal efficiency was calculated in two different ways during the steady state periods. First, by applying

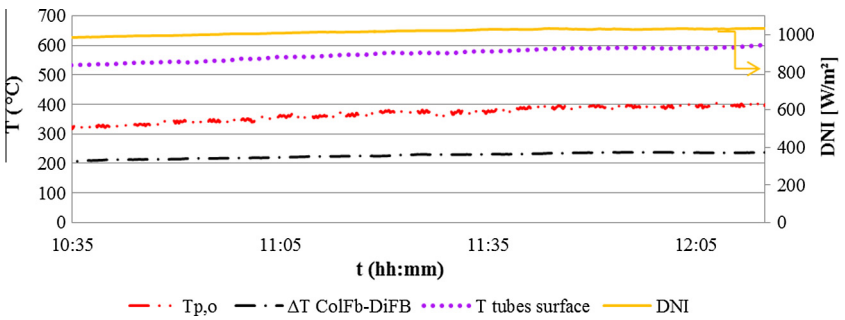

Fig. 13. Mean solid outlet temperature, temperature increase between ColFB and DiFB and direct normal irradiation (DNI) versus time.

Equations (2)–(5) to time-dependent values of the concerned data (DNI, $T_{p,ColFB}$, $T_{p,DiFB}$, F_p, $c_{p,p}$), instantaneous values of η_{th} were determined and then averaged over time. Second, by calculating η_{th} with Equations (2)–(5) from time-averaged values of the measured data. The difference between the values obtained by both ways was less than 0.05%, with a mean value of 0.01%. This shows the steady state definition consistency.

Fig. 14 plots the thermal efficiency η_{th} as a function of the solid flux for the three considered solar power ranges at the cavity inlet. The thermal efficiency η_{th} ranges from 50 to 90%, and in all cases it increases with the solid flux. In the plot, information on the measurement uncertainty is given through error bars for each experimental point. The error was estimated as follows:

From Eq. (2), the relative error on the thermal yield η_{th} is

$$\frac{\Delta\eta_{th}}{\eta_{th}} = \frac{\Delta\phi_{DPS}}{\phi_{DPS}} + \frac{\Delta\phi_{in}}{\phi_{in}} \quad (6)$$

And from Eq. (4), the relative error on the heat flux $\phi_{DPS16Tubes}$ is

$$\frac{\Delta\phi_{DPS}}{\phi_{DPS}} = \frac{\Delta F_p}{F_p} + \frac{\Delta c_{p,p}}{c_{p,p}} + 2\frac{\Delta T_p}{T_p} \quad (7)$$

The uncertainty ΔF_p was estimated from an experimental correlation F_p versus $\Delta P_{DiFB\text{-}Tank}$. ΔF_p was taken as the maximal difference between the measured value and the value calculated with the correlation; the relative error on F_p was always less than 5%. The relative error on $c_{p,p}$ (issued from the NIST database) was 5%. The uncertainty on sheathed K thermocouple indications (T_p) was ±2.5 °C up to 333 °C and ±0.0075 × T (in °C) over 333 °C. Based on the accuracy of the 25 mm calorimeter used for flux density measurements, the relative error on ϕ_{in} was estimated to 2%.

3.5. Transient state analysis

3.5.1. Particle temperature

During transient periods, the solid temperature reached 755 °C at the outlet of one of the hottest tubes and the mean temperature reached 590 °C at the tubes' outlet (Fig. 15), with a 30 kg/s.m^2 solid mass flux, and an average solar power at the cavity entrance 83 kW$_{th}$. Fig. 15 shows the solid temperature distribution at the tube outlet and the mean temperature of the 16 tubes. The solar flux heterogeneity limited the mean temperature reached by the particle flow, similarly to the steady state periods. This is why the solid temperature overpasses 700 °C only at the outlet of tubes 5 and 12, and it overpasses 600 °C in only 5 out of 16 tubes. The difference in DPS temperature between the hottest and coldest tubes was as high as 246 °C in this case.

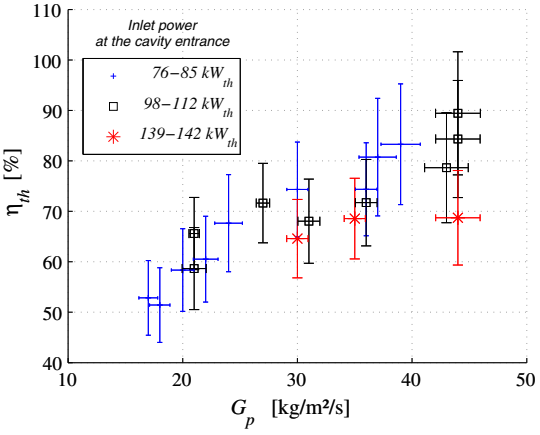

Fig. 14. Solar receiver thermal efficiency as a function of the solid flux for the three considered solar powers ranges at the cavity aperture.

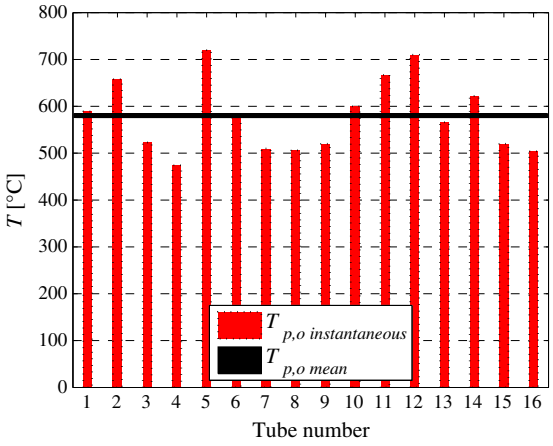

Fig. 15. Instantaneous solid temperatures at the tube outlets and their average during a transient experiment (solid flux rate = 30 kg/m^2.s, aeration = 0.09 N m^3/m^2.s).

3.5.2. System response to DNI changes

The system response to Direct Normal Irradiation (DNI) variations was studied when irradiation conditions changed, either quickly (cloud) or slowly (sunset approach). The system stands very well irradiation fluctuations; small clouds have very little impact on the mean particle temperature at the receiver (tubes) outlet. Fig. 16 displays the transient DNI and the solid and wall temperatures for an experiment with variable irradiation conditions. The tube surface temperature is the average of all values recorded by the thermocouples welded on the tubes. Between 12:48 and 12:53, the DNI drops under 150 W/m^2, and the tubes' surface temperature falls from 397 °C to 232 °C (ΔT = 165 °C), while the DPS temperature at the tubes outlet drops down from 257 °C to 200 °C (ΔT = 57 °C), and the solid temperature in the ColFB varies from 245 °C to 226 °C (ΔT = 19 °C). The particle temperature drops, both at the tube outlets and in the ColFB, are lower than the wall temperature drop. This is because the system is self-regulated with respect to solid mass flow rate. At 12:48, when the DNI drops down, the solid mass flow rate decreases also without any operator's action from 1.25 T/h to 0.96 T/h. When the sky clears again, at about 13:00, the solid flow rate rises from 0.96 T/h to 1.2 T/h. Actually, the solid flow rate decrease limits the solid temperature drop when the wall temperature drops. The thermal inertia of the particles in the ColFB provokes a lower temperature drop than at the tube outlets. The reason why the solid flow rate decreases when the DNI and temperature drop is as follows. The temperature drop provokes an air density increase. Consequently, the air velocity decreases, thus the voidage decreases and the DPS hydrostatic pressure in the tube increases. The pressure drop on the tubes comprises the hydrostatic pressure, which is its main component, and the friction pressure loss. The total pressure drop remains constant since the pressure in the DiFB freeboard is controlled by the regulation valve. To maintain the pressure equilibrium, the friction pressure loss must decrease when the hydrostatic pressure increases. A friction pressure loss decrease means a solid velocity and mass flow rate decrease.

3.5.3. System response to changes on solid mass flow rate

Fig. 17 shows the system response when the operator changes purposely the mass flow rate, for the mean temperature of tube walls, the solid mean temperature at the tube outlets, and the temperature increase between DiFB and ColFB; it also indicates the recorded DNI. Table 7 shows the three steady state periods reached during the experiment plotted in Fig. 17. During the steady state period 'I', a 36 kg/m^2.s solid mass flux leads to

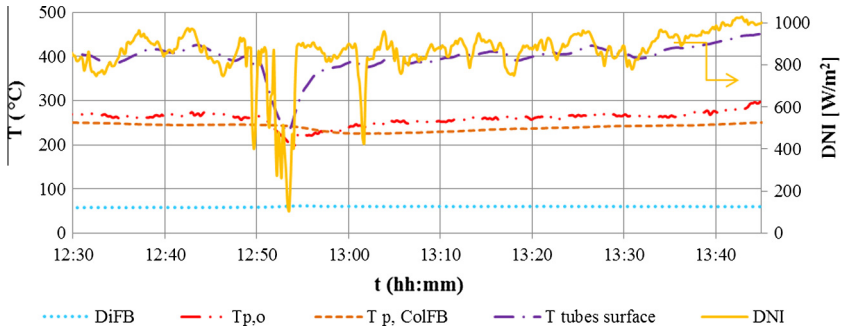

Fig. 16. Transient DNI and temperatures (solid mass flow rate = 1.25; 0.96; 1.2 T/h; mass flux = 31; 24; 30 kg/m^2.s; mean normalized solar power at the cavity entrance = 77 kW_{th}).

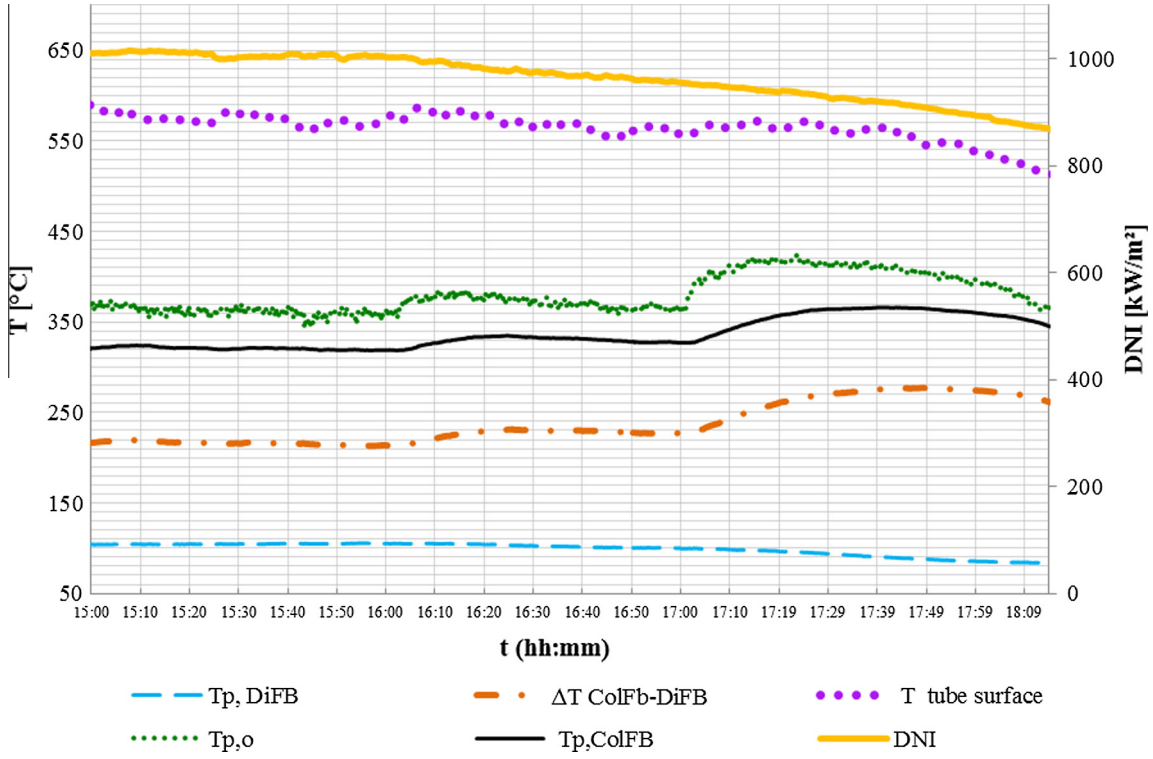

Fig. 17. Transient solid mean temperature in the DiFB, at the tubes outlets, in the ColFB, wall mean temperature, particle temperature increase between DiFB and ColFB, and DNI.

Table 7
Operating parameters and results of the experiment shown in Fig. 17.

Steady state	Time of start/end (hh:mm)	G_p (kg/m^2.s)	ϕ_{in} (kW_{th})	$\Delta T_{p,DiFB\text{-}ColFB}$ (°C)	$T_{p,o}$ (°C)
I	15:00/16:00	36	108	216	359
II	16:10/17:00	31	104	228	369
III	17:10/18:15	21	98	269	403

$\Delta T_{DiFB\text{-}ColFB}$ = 216 °C. When the mass flux decreases from 36 to 31 kg/m^2.s (14% reduction) by changing the rotary valve frequency, $\Delta T_{p,DiFB\text{-}ColFB}$ increases from 216 to 228 °C, that is a 6% increase. When the mass flux is reduced to 21 kg/m^2.s, the temperature increase grows to 269 °C, which means a 23% increase of $\Delta T_{p,DiFB\text{-}ColFB}$, for 48% solid flux decrease, in comparison to the initial steady state 'I'.

The solid flow rate decrease makes the particles spend more time in the recycling part of the loop (CoolFB, screw conveyor, storage) where heat is lost. Moreover, at lower flow rate, the heat transfer coefficient in the tubes is lower, which means that the total power received by the DPS is lower. These combined causes lead to colder particles being fed to the DiFB and thus to the DiFB temperature decrease. In addition, the DNI is progressively decreasing. All this leads to the slow decrease of $T_{p,o}$ and $T_{p,ColFB}$, with the fall of $T_{p,ColFB}$ mitigated by the bed thermal inertia. Since $T_{p,DiFB}$ and $T_{p,ColFB}$ both decrease at the same time during periods when the solid flow rate is kept constant, $\Delta T_{ColFB\text{-}DiFB}$ is stable during these periods. Finally, the steeper fall of DNI at 18:00 explains the rapid $T_{p,o}$ decrease at the end of the test.

4. Discussion and conclusion

A series of on-sun runs of a 50–150 kW_{th} multi-tube solar receiver with dense particle suspension as HTF was performed. On-sun operation of the pilot rig was achieved during several full days, with continuous particle circulation in closed loop and more than 30 h at steady state. The rig was steadily operated with particle temperature increase in the range 137–335 °C for a 1 m irradiated tube height. For the hottest case, the mean outlet temperature was higher than 490 °C at the receiver outlet during steady state periods, and it was higher than 590 °C during transient periods. The particles were even heated higher than 700 °C in the hottest tubes, because of the heterogeneous concentrated solar flux, inherent to the solar furnace.

In this study that involved a cavity receiver, the calculated receiver thermal yield was as high as 90% for a 44 $kg/m^2.s$ solid mass flux and a 370 °C mean particle temperature at the tubes outlet.

During transient periods, the system showed a self-regulation capacity, decreasing and increasing the solid flow rate when the DNI dropped or rose. This behavior is very interesting for power plant operation.

The heat lost by the process through the air circulation is extremely limited. The sum of the energy contained in the air heated in the tubes and of that used for heating the fluidization air in the collector fluidized bed represents less than 2% of the power transmitted to the DPS in the most unfavorable case (high temperature increase between DiFB and ColFB, low solid flow rate) and the average on all experimental runs is less than 1%.

The air velocity in the system is very low. Taking the air expansion with temperature into account, a 0.2 m/s maximum air superficial velocity in tube was calculated accounting for both fluidization and aeration air. In addition to a negligible particle attrition, this leads to very low friction pressure losses in the tubes. Therefore, the pressure drop in the tubes is essentially due to the particles' weight, it is about 116 mbar/m. For very small air mass flow rates, the power used for the air circulation is very low (lower than in circulating fluidized beds and lower than the power needed for molten salts circulation (Boissière, 2015). Furthermore, the analysis of a 10 MW_{th} DPS receiver, carried out by Gallo et al. (2015) showed that the parasitic consumption for the receiver amounts to a total of 19.7 kW_e of which 18.9 kW_e are for particle transport.

These experimental results prove the feasibility of the multi-tube dense particle suspension receiver concept and its capacity to operate at high temperature in realistic conditions. This clearly opens the possibility of using high efficiency thermodynamic cycles at temperatures higher than current technologies. The technical-economical analysis of a 50 MW_e CSP plant based on the use of DPS as HTF indicated an increase of 5.5 percentage-points in the thermal conversion efficiency, compared to a typical dry-cooled molten-salt power plant (Spelling et al., 2015). Therefore the dense particle suspension solar receiver appears to be a promising new technology, but several elements must be investigated for the process scaling-up.

The DPS flow in tubes is influenced by the tubes' dimensions. The tube diameter plays a role in relation with the size of bubbles in the DPS. It is expected to have very little influence in the range 20–50 mm. However, for an inside diameter above 50 mm, the bubbles will be smaller than the tube diameter and, therefore, their passage will leave zones where particles are not well mixed, which should decrease the wall-to-suspension heat transfer. The tubes will have to be higher in industrial applications. Higher tubes mean higher pressure drop and higher temperature increase, and therefore a significant air expansion. Plug flow may result from this behavior. Consequently, experiments and numerical simulation should be developed to understand the variation of DPS characteristics in long hot tubes.

Acknowledgements

This study was performed in the framework of the CSP2 Project - Concentrated Solar Power in Particles", funded by the European Commission (FP7, Seventh Framework Programme, Project N° 282 932). It was also by the Programme «*Investissements d'avenir*» of the *Agence Nationale de la Recherche* (National Agency for Research) of the French State under award number "ANR-10-EQP X-49-SOCRATE" named "SOCRATE" and under award number "ANR-10-LABX-22-01" named SOLSTICE.

References

Baharoon, D.A., Rahman, H.A., Wan Omar, W.Z., Fadhl, S.O., 2015. Historical development of concentrating solar power technologies to generate clean electricity efficiently- a review. Renew. Sustain. Energy Rev. 41, 996–1027.

Barlev, D., Vidu, R., Stroeve, P., 2011. Innovation in concentrated solar power. Sol. Energy Mater. Sol. Cells 95, 2703–2725.

Benoit, H., Pérez López, I., Gauthier, D., Sans, J.-L., Flamant, G., 2015. On-sun demonstration of a 750 °C heat transfer fluid for concentrated solar systems: dense particle suspension in tube. Sol. Energy 118, 622–633.

Boissière, B., 2015. Étude hydrodynamique et thermique d'un nouveau concept de récepteur solaire à suspensions denses gaz-particules (Hydrodynamic and thermal study of a new concept of solar receiver using dense gas-particle suspensions). PhD thesis, Institut National Polytechnique de Toulouse (INP Toulouse).

Boissière, B., Ansart, R., Gauthier, D., Flamant, G., Hemati, M., 2015. Experimental hydrodynamic study of gas-particle dense suspension upward flow for applications as new heat transfer and storage fluid. Can. J. Chem. Eng. 93, 317–330.

BrightSource. Ivanpah project facts. (available at: <http://www.brightsourceenergy.com/stuff/contentmgr/files/0/8a69e55a233e0b7edfe14b9f77f5eb8d/folder/ivanpah_fact_sheet_3_26_14.pdf>).

CSP2 Project. Available at <http://www.csp2-project.eu/> (accessed December 05, 2015).

Dunham, M.T., Iverson, B.D., 2014. High-efficiency thermodynamic power cycles for concentrated solar power systems. Renew. Sustain. Energy Rev. 30, 758–770.

Fernández-García, A., Zarza, E., Valenzuela, L., et al., 2010. Parabolic- trough solar collectors and their applications. Renew. Sustain. Energy Rev. 14 (7), 1695–1721.

Flamant, G, Hémati, M., 2010. Dispositif collecteur d'énergie solaire, October 22 (2010), French Patent N° 10 58565 2.

Flamant, G., Gauthier, D., Benoit, H., Sans, J.-L., Garcia, R., Boissière, B., Ansart, R., Hemati, M., 2013. Dense suspension of solid particles as a new heat transfer fluid for concentrated solar thermal applications: on sun proof of concept. Chem. Eng. Sci. 102, 567–576.

Gallo, A., Spelling, J., Romero, M., González.-Aguilar, J., 2015. Preliminary design and performance analysis of a multi-megawatt scale dense particle suspension receiver. Energy Proc 69, 388–397.

García-Triñanes, P., Seville, J.P.K., Boissière, B., Ansart, R., Leadbeater, T.W., Parker, D. J., 2016. Hydrodynamics and particle motion in upward flowing dense particle suspensions: Application in solar receivers. Chem. Eng. Sci. 146, 346–356.

Geldart, D., 1973. Types of gas fluidization. Powder Technol. 7 (5), 285–292.

Ho, C.K., Iverson, B.D., 2014. Review of high-temperature central receiver designs for concentrating solar power. Renew. Sustain. Energy Rev. 29, 835–846.

International Energy Agency, 2011. Renewable Energy Technologies: Solar Energy Perspectives. ORCD/IEA Publications, Paris.

Munro, 1997. Material properties of a sintered a-SiC. J. Phys. Chem. Ref. Data 26 (4), 1195–1203.

NREL data base <http://www.nrel.gov/csp/solarpaces/project_detail.cfm/>.

RED electrica de España (REE), 2014. The Spanish Electricity System – Complete Report 2013, RED, Madrid, Spain, <http://www.ree.es/es/publicaciones/sistema-electrico-espanol/informe-anual/informe-del-sistema-electrico-espanol-2013>.

RED electrica de España (REE), 2015. The Spanish Electricity System – Complete Report 2014, RED, Madrid, Spain, <http://www.ree.es/es/publicaciones/sistema-electrico-espanol/informe-anual/informe-del-sistema-electrico-espanol-2014>.

SolarReserve. Crescent Dunes. <http://www:solarreserve:com/en/global-projects/csp/crescent-dunes>.

Spelling, J., Gallo, A., Romero, M., González-Aguilar, J., 2015. A high-efficiency solar thermal power plant using a dense particle suspension as the heat transfer fluid. Energy Proc 69, 1160–1170.

Technology Road Map, 2014. Solar thermal electricity. IEA Publications, Paris.

Thonglimp, V., Hiquily, N., Laguerie, C., 1984. Vitesse minimale de fluidisation et expansion des couches fluidisées par un gaz (Minimum fluidization velocity and gas-fluidized layers expansion). Powder Technol. 38 (3), 233–253.

Turzo G., 2013. Transport par fluidisation en phase hyperdense: amélioration technologique, modélisation et dimensionnement (Hyperdense phase transport by fluidization: technological improvement, modeling and design). PhD thesis, University of Toulouse.

Zhang, H.L., Baeyens, J., Degrève, J., Cacères, G., 2013. Concentrated solar power plants: review and design methodology. Renew. Sustain. Energy Rev. 22, 466–481.

Zhang, H., Degrève, J., Baeyens, J., Wu, S.-Y., 2016. Powder attrition in gas fluidized beds. Powder Technol. 287, 1–11.

Zhang, H., Benoit, H., Gauthier, D., Degrève, J., Baeyens, J., Pérez, López.I., Hemati, M., Flamant, G., 2016. Particle circulation loops in solar energy capture and storage; gas-solid flow and heat transfer considerations. Appl. Energy 161, 206–224.